Nano-Micro Letters
e-ISSN 2150-5551
CN 31-2103/TB
ARTICLE
https://doi.org/10.1007/s40820-026-02358-7

Cite as
Nano-Micro Lett.
(2027) 19:63

Received: 23 April 2026
Accepted: 10 August 2026
© The Author(s) 2026

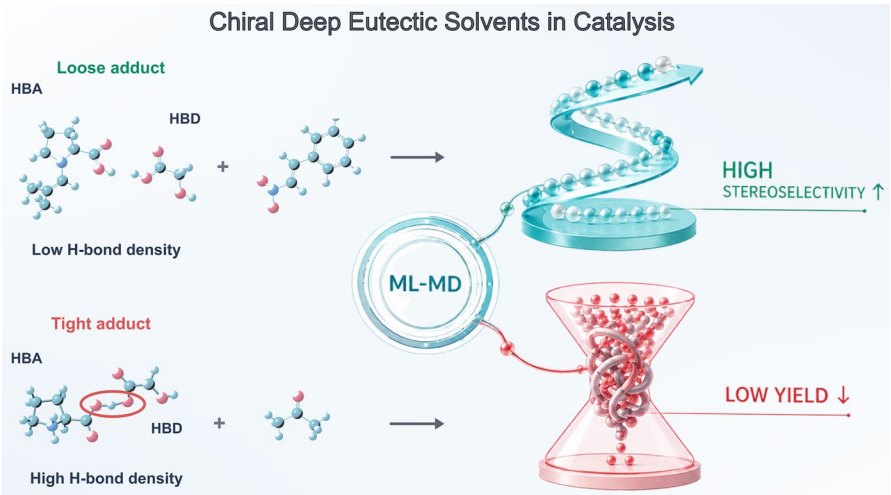
Predicting Asymmetric Organocatalysis via Machine-Learning-Driven Molecular Dynamics of Chiral Deep Eutectic Solvents

Michele Tomasini[1], Matteo Tiecco[2], Diego A. Alonso[3], Luca Fortunato[4], Laura Falivene[1] ✉

HIGHLIGHTS

- Machine-learning molecular dynamics reveals how hydrogen-bond dynamics in chiral deep eutectic solvents dictate catalytic performance.
- Hydrogen-bond descriptors provide a predictive framework for optimizing catalyst design.
- Atomistic insights bridge solvent organization with macroscopic reactivity.

ABSTRACT Deep eutectic solvents (DESs) serve as sustainable, low-volatility, and bio-derived alternatives to conventional organic media, aligning with the demand for green chemical processes. Beyond their role as solvents, they offer transformative potential as integrated catalytic platforms, yet the molecular determinants of their performance remain poorly understood. This study employs machine-learning-driven molecular dynamics combined with density functional theory to investigate the structure and dynamics of chiral deep eutectic solvents in asymmetric catalysis. Simulations reveal that overly persistent hydrogen-bond networks within DES components impede key reaction steps and intermediate formation, reducing efficiency. Conversely, more labile networks preserve molecular flexibility, facilitating substrate activation and enhancing conversion. Furthermore, these networks compete with interactions controlling substrate orientation, thus influencing stereocontrol. By connecting microscopic hydrogen-bond dynamics to macroscopic performance, this work provides atomistic insight into structure–reactivity relationships. The findings define a quantitative computational framework that uses hydrogen-bond descriptors to predict catalytic efficiency. This approach demonstrates the utility of artificial intelligence-driven methodologies for the accelerated optimization and rigorous benchmarking of catalytic systems, offering a mechanism-based strategy for the rational design of next-generation organocatalytic media.



KEYWORDS Sustainable catalyst design; Machine-learning molecular dynamics; Chiral deep eutectic solvents; Asymmetric organocatalysis; Hydrogen-bonding descriptors

✉ Laura Falivene, lafalivene@unisa.it
[1] Department of Chemistry and Biology, University of Salerno, Via Ponte don Melillo, 84084 Fisciano, Italy
[2] Chemistry Interdisciplinary Project (ChIP), School of Pharmacy, University of Camerino, Via Madonna delle Carceri, 62032 Camerino, MC, Italy
[3] Department of Organic Chemistry and Organic Synthesis Institute (ISO), Alicante University, Apdo. 99, 03080 Alicante, Spain
[4] Department of Civil, Building and Environmental Engineering, University of Napoli Federico II, Via Claudio 21, 80125 Napoli, Italy

Published online: 23 November 2026

1 Introduction

The development of sustainable chemical processes is a central pillar of modern green chemistry, necessitated by the urgent need to replace volatile, toxic, and petroleum-derived organic solvents [1]. Deep Eutectic Solvents (DESs) have emerged as a transformative class of "designer media" that align with these sustainability goals. These systems, formed by the simple mixing and heating of a hydrogen-bond donor (HBD) and a hydrogen-bond acceptor (HBA), are characterized by low-volatility, facile recyclability, and high atom economy in their preparation [2, 3]. Their unique structural characteristics and distinctive properties make them especially intriguing and versatile for a wide range of applications [4, 5]. Importantly, unlike many conventional ionic liquids, which often require multi-step and waste-intensive synthesis, many DESs can be readily prepared from renewable feedstocks, such as L-proline and glycerol. However, the “greenness” of a solvent is not merely a function of its low toxicity, but also of its efficiency in facilitating chemical transformations. To this extent, when the components of a DES possess intrinsic catalytic properties, such as acidic, basic, or reducing functionalities, the resulting medium displays emergent catalytic behaviour [6]. In such systems, the catalytic performance is governed not only by the intrinsic reactivity of their constituents, but also by the dynamic structuring of the solvent environment within an extended hydrogen-bonded network, which modulates the accessibility, orientation, and stabilization of reactive sites [7]. In this context, DESs have largely been explored as tunable media in which noncovalent interactions can strongly influence molecular organization and mesoscale behaviour [8–12]. These studies highlight how subtle changes in the solvent environment can lead to pronounced structural and dynamical effects, underscoring the importance of molecular-level descriptors of solvent organization.

In chiral DESs (cDESs), organocatalysts embedded within the solvent matrix can promote stereoselective transformations [13]. In these systems, the catalytic species is an integral part of the structured solvent and must often be sufficiently “released” from the surrounding hydrogen-bond network to act effectively. Catalytic efficiency and stereocontrol therefore emerge from a subtle interplay between substrate–solvent interactions, hydrogen-bond dynamics, and the evolving supramolecular organization of the medium [14]. Depending on the specific interaction pattern, the solvent network can either hinder substrate activation or, conversely, enhance stereoselectivity, in some cases reaching very high or even complete levels. This intimate coupling between solvent and catalyst renders cDESs a distinctive form of organocatalysis [15, 16], which does not fit neatly into conventional categories such as transition-metal catalysis, classical organocatalysis, or biocatalysis. Consequently, detailed insight into the molecular-level structure and dynamics of these systems is essential to rationalize their catalytic behaviour, interpret experimental observations, and elucidate the underlying mechanisms, thereby guiding rational design and ultimately enabling predictive control over the organocatalytic activity of these innovative liquid systems.

Computational modelling [17–25] offers a powerful avenue for unravelling structure-reactivity relationships, enabling systematic exploration of chemical space while minimizing trial-and-error experimentation. However, in highly structured DES environments, a complete mechanistic investigation becomes computationally demanding, as it requires extensive sampling of solvent configurations, intermediates, and transition states. In addition, static calculations based on a limited set of representative structures may not fully capture the dynamic and cooperative nature of these systems, where the hydrogen-bond network continuously evolves and shapes the local catalytic environment. Molecular dynamics (MD) simulations, instead, capture the temporal evolution of solvent networks, providing access to time-resolved dynamical behaviour that is not accessible through conventional static calculations. Classical MD relies on predefined force fields and can provide valuable structural insights; however, its reliability depends strongly on the quality and transferability of the interaction model. This is particularly relevant for DESs, whose liquid structure is controlled by a delicate balance of hydrogen bonding, electrostatics, dispersion, polarization, charge transfer, and, in some cases, proton sharing or proton-transfer events. Several studies have shown that DES simulations often require system-specific parametrization, charge scaling, or explicit polarization to reproduce experimental observables and first-principles reference data [26–31]. In contrast, ab initio molecular dynamics (AIMD) offers quantum-mechanical accuracy without relying on predefined force fields; however, it remains constrained by accessible system sizes and

© The authors
https://doi.org/10.1007/s40820-026-02358-7

simulation timescales. These limitations are especially important for DESs, where slow collective rearrangements and extended hydrogen-bond networks require larger simulation boxes and longer sampling times.

Machine-learning (ML) methods overcome these limitations by capturing complex, nonlinear relationships between molecular descriptors and target properties directly from data, providing a powerful framework for predicting molecular properties and uncovering hidden patterns in chemical systems. As a result, ML has become an increasingly important tool across materials science and molecular design, where it is being applied to accelerate materials discovery and predict physicochemical properties [32–34]. In asymmetric catalysis, recent AI- and ML-assisted approaches have successfully predicted enantioselectivity, reaction yields, and stereochemical outcomes using descriptor-based models, graph neural networks, and deep-learning frameworks informed by chemical and mechanistic knowledge [35–37].

At the same time, the application of ML in chemistry has expanded to the dynamical modelling of molecular systems through machine-learning potentials (MLPs) [38–42] that provide an efficient framework for performing atomistic molecular dynamics simulations with near ab initio accuracy at a computational cost that allows simulations of large, complex systems over experimentally relevant timescales [43–47]. Importantly, MLPs do not require the predefinition of empirical force-field parameters, making them well suited for exploring novel and unconventional DES formulations. Together, these approaches complement traditional methods, facilitating fast screening, inverse design, and data-driven insights that can accelerate the discovery and optimization of DESs as catalysts. Although MD simulations have been extensively employed to investigate ionic liquids (ILs) [48–51], DESs, particularly non-ionic or chiral systems, have only recently attracted significant attention [27, 52–55]. To date, most computational studies have focused on choline chloride-based DESs [19, 20, 39, 56, 57], leaving non-ionic and zwitterionic systems largely unexplored, and a molecular-level understanding of DESs in the context of catalysis is essentially absent.

Here, we present a machine-learning-driven molecular dynamics study of a series of L-proline- and quaternary ammonium pyrrolidine-based cDESs, complemented by density functional theory (DFT) calculations. A pre-trained ML interatomic potential is employed to sample their dynamic supramolecular organization and characterize the hydrogen-bond networks and noncovalent interactions that underpin catalytic behaviour, enabling the extraction of mechanistically meaningful descriptors. This approach enables a direct connection between the microscopic structure and dynamics of cDESs and their macroscopic catalytic performance, including activity and stereoselectivity. The resulting atomistic insight reveals how subtle changes in solvent organization modulate the catalytic environment, providing a predictive, mechanism-based framework for the rational design of cDESs for asymmetric transformations, thereby reducing reliance on extensive trial-and-error experimentation. By moving beyond empirical screening, this work establishes DESs as engineerable catalytic media whose properties can be systematically tuned and predicted. Given the vast combinatorial space of DES components, such an approach represents a decisive step towards the knowledge-driven design of sustainable catalytic platforms.

2 Computational Methods

2.1 Molecular Dynamics Simulations

All MD simulations in this study were conducted with the LAMMPS package [58], utilizing preferred potential framework (PFP) as implemented in Matlantis [59]. This approach leverages a neural network model inspired by TeaNet [60], which processes atomic arrangements as high-dimensional inputs to predict potential energy values. The network was previously trained on datasets comprising pairs of atomic structures and their corresponding energies, derived from AIMD simulations performed with DFT. The force field, model version of estimator, and calculation model used are PFP, v5.0.0, and CRYSTAL_PLUS_D3 with Hubbard and dispersion corrections, respectively.

To directly evaluate the structural accuracy of the Matlantis MLIP, we compared MLIP-optimized molecular clusters with DFT-optimized reference geometries (Tables S1 and S2).

Initial configurations of the DES mixtures were generated using Packmol [61], placing 100 molecules of the HBA and 100 molecules of the HBD randomly within the simulation box. Additional simulations were performed for reactive

systems by arranging 50 molecules of the HBA in its enamine form together with 50 molecules of the HBD and 50 molecules of *trans*-β-nitrostyrene. The initial dimensions of the cubic simulation cell were set to $35 \times 35 \times 35$ Å^3. Periodic boundary conditions were applied in all three spatial directions. An initial minimization was performed to eliminate close contacts and achieve the minimum energy structure for further simulations. Subsequently, the system underwent equilibration at 300 K for 5 ps under the NVT ensemble. Temperature control was achieved via the Berendsen thermostat [62] with a coupling time of 0.1 ps. Subsequently, an additional equilibration was performed under the NPT ensemble. Finally, the equilibrated system was employed for production simulations over 100 ps under the NPT ensemble. To maintain a pressure of 1 atm, the Berendsen barostat was applied with a coupling time of 1.0 ps. The equations of motion were integrated using the Verlet algorithm [63] with a time step of 1 fs. MDAnalysis tools [64] were employed for the analysis, and the visualization of the simulation data was performed using the VMD program [65].

2.2 DFT Calculations

Representative molecular clusters were extracted from selected snapshots of the MD trajectories and used as input for static DFT calculations. All DFT computations were performed using the Gaussian 16 software package. Geometry optimizations were carried out employing the dispersion-corrected B3LYP-D3 [66–69] functional in combination with the 6-31G(d) basis set [70, 71].

Analytical frequency calculations were performed at the same level of theory to characterize the nature of the stationary points and to confirm the optimized structures as true minima on the potential energy surface. To assess the robustness of the computational results with respect to the choice of basis set and density functional, additional validation calculations were performed on selected representative clusters. In particular, geometry optimizations were repeated using the larger and more flexible 6-311++G(d,p) basis set [71–73]. Selected systems were also investigated at the ωB97X-D/def2-TZVP level of theory [74, 75], a method particularly well suited for the accurate description of noncovalent interactions.

2.3 Noncovalent Interactions (NCI) Analysis

The NCI plots developed by Contreras-Garcia [76, 77] and coworkers were generated by examining the DFT-calculated wavefunctions with Multiwfn [78] software, and the 3D structures were visualized using VMD software.

The NCI index is a powerful visualization tool that provides insights into noncovalent interactions by mapping regions of electron density and its gradients. This method identifies both favourable and unfavourable interactions within a molecular system. Strong attractive interactions, such as hydrogen bonds, are shown in blue, weak van der Waals interactions appear in green, and repulsive interactions are represented in red.

3 Results and Discussion

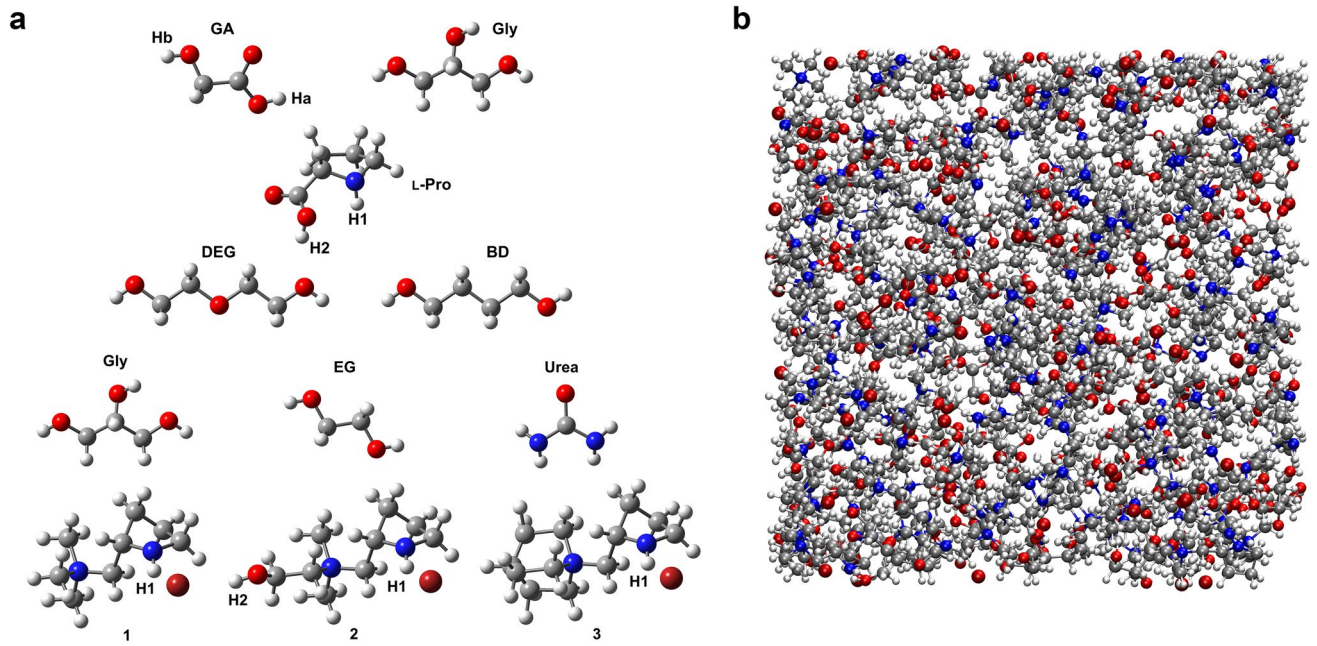
Two representative literature examples were selected as computational case studies to unravel how molecular composition shapes microscopic organization and governs catalytic performance. The first set features L-proline (L-pro) as the HBA, paired with glycerol (Gly), glycolic acid (GA), diethylene glycol (DEG), or 1,4-butanediol (BD) as HBDs, and was experimentally tested in the conjugate addition of butanone to *trans-β*-nitrostyrene [79]. The second set comprises DESs based on quaternary ammonium salts derived from L-proline (compounds **1**-**3**, Scheme 1) as HBAs, combined with Gly, ethylene glycol (EG), or urea as HBDs, and was evaluated in the conjugate addition of cyclohexanone to *trans*-β-nitrostyrene [80].

Experimental results (Table 1) reveal striking differences in catalytic efficiency depending on both HBA and HBD identity. Among the L-proline-based DESs, **L-pro/Gly**, **L-pro/DEG**, and **L-pro/BD** achieve high conversions (92-95%), whereas **L-pro/GA** reaches only 15%. In contrast, the quaternary ammonium-based DESs exhibit consistently outstanding performance, achieving >99% conversion in shorter reaction times, with the sole exception of **1/Gly**.

The systems were simulated using ML-MD, which enabled a more rapid exploration of previously untested DESs without requiring the development of new force fields.

To ensure methodological reliability, the simulation protocol was validated by comparing the simulated densities with experimentally measured values. Density comparison is a widely used benchmark for validating molecular

© The authors
https://doi.org/10.1007/s40820-026-02358-7



Scheme 1 **a** Schematic representation of the cDESs considered with the corresponding numbering. **b** A structural model of one of the examined mixtures. Atoms are coloured as follows: carbon in silver, hydrogen in white, oxygen in red, nitrogen in blue, bromine in dark red

simulations of liquid systems and deep eutectic solvents [81], as it directly probes the ability of the force field and simulation protocol to reproduce liquid packing and cohesive interactions. In addition to the L-pro/GA system at a 1:1 molar ratio, for which literature density values are available [82], the benchmark was extended to the L-pro/Gly and L-pro/DEG systems using experimental densities measured by some of us (Table S3). The simulated densities are in good agreement with the corresponding experimental values, with deviations generally close to or within 5% across the investigated systems. This level of agreement supports the ability of the ML-MD approach to accurately capture the bulk structural and dynamical properties of the studied DESs.

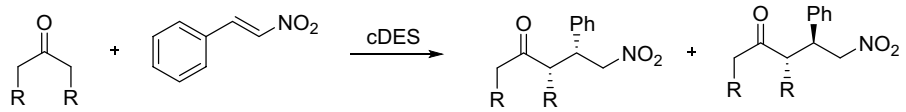
MD trajectories (Table S4) were analysed using site–site radial distribution functions (RDFs) [83, 84] to unravel the microscopic organization and dominant intermolecular interactions in the systems. RDFs provide a direct, quantitative measure of local structuring, where more intense peaks indicate a higher probability of contact between the selected sites. This approach reveals how specific interactions govern the liquid-state architecture and dictate the spatial arrangement of molecular fragments.

For each component, chemically meaningful atomic sites were selected to compute RDFs (see Table S5) and systematically probe all relevant interactions. In particular, hydrogen bonding [85] and ionic coordination were investigated by analysing the distributions between: (i) HBD hydrogen atoms and ether atoms of the HBA, (ii) HBA hydrogen atoms and ether atoms of the HBD, and (iii) the anion and key hydrogen atoms on both HBA and HBD moieties in quaternary ammonium salt-based systems. This analysis provides a coherent structural fingerprint of each DES, allowing characteristic coordination motifs to be identified and correlated with trends in organocatalytic performance. Comparison of the RDFs calculated over different trajectory blocks was used to assess statistical convergence and identify any time-dependent variations in the local structure (Supporting Information).

3.1 Chiral L-Proline-Based DESs

In the **L-pro/Gly** system, RDF analysis highlights two pronounced interactions between the N atom and hydrogen atoms at 1.02 (H1) and 1.08 Å (H2), with g(r) peaks reaching ~160-170, characteristic of covalent-like contacts

Table 1 Asymmetric conjugate addition of ketones to *trans*-β-nitrostyrene employing cDESs



System	HBA	HBD	Conversion (%)
L-pro/Gly	L-proline	Glycerol	>95[a]
L-pro/GA	L-proline	Glycolic acid	15[a]
L-pro/DEG	L-proline	Diethylene glycol	92[a]
L-pro/BD	L-proline	1,4-Butanediol	>95[a]
1/Gly	1	Glycerol	17[b]
2/EG	2	Ethylene glycol	>99[b]
3/Urea	3	Urea	>99[b]

[a] Butanone was used as ketone. T = 30 °C, t = 5 d. cDES = 0.5 g. [b] Cyclohexanone was used as ketone. T = rt, t = 18 h. Cyclohexanone (0.2 mmol), β-nitrostyrene (0.1 mmol), chiral liquid/limiting reagent mass ratio of 5/1.

(Fig. 1a). These data indicate protonation of the L-proline nitrogen via proton transfer from the carboxyl group, revealing a key structural motif that likely underpins the hydrogen-bond network and stabilizes the local organization of the DES. Such interactions provide a microscopic basis for the catalytic performance observed in the Michael addition reaction. In particular, the formation of a quaternary ammonium N^+ centre reduces the nitrogen's nucleophilicity, hindering its reaction with the ketone substrate to form the enamine, a key intermediate in the catalytic cycle. This structural effect directly limits catalytic turnover, rationalizing the experimentally observed need for longer reaction times and elevated temperatures in these DESs compared to quaternary ammonium salt-based systems. These findings highlight how modifications of ammonium protonation state can be strategically leveraged to control both intermediate formation and overall reactivity.

The analysis further highlights key HBD–HBA interactions: H2 interacts with the glycerol oxygen (1.72 Å, g(r) ≈ 3, violet curve in Fig. 1b), while the proline $–COO^-$ oxygen engages more strongly with glycerol –OH hydrogens (1.72 Å, g(r) ≈ 5, green curve in Fig. 1b). Together, these interactions reveal a cooperative hydrogen-bonding network in which the L-proline moiety acts both as a proton donor and a proton acceptor.

We extended this analysis to probe the effect of substituting glycerol with glycolic acid as the HBD, while retaining L-proline as the HBA. The intramolecular interactions within proline remain largely preserved: N remains protonated, forming covalent bonds with H1 and H2, which in turn engage the $–COO^-$ group, closely resembling the glycerol system. However, replacing glycerol with glycolic acid significantly modifies intermolecular interactions. The N-H proton exhibits reduced interaction strength with the oxygen atoms of GA (violet curve, Fig. 2; 1.72 Å, g(r) ≈ 1.5, versus ≈3 in the Gly system, Fig. 1b). Moreover, comparison of the green curves in Figs. 1b and 2 show that the ~1.6 Å peak, corresponding to interactions between the L-proline oxygen and HBD–OH hydrogens, persists, while GA introduces a pronounced new peak near 1 Å, arising from the HBD carboxylic –OH (Ha) and indicative of partial hydrogen transfer to L-proline.

The most probable MD configurations were subsequently re-optimized using DFT. For each system, a representative fragment comprising two HBD and two HBA molecules was selected. NCI analyses were then performed to visualize the hydrogen-bonding and van der Waals networks (Figs. 3 and S36).

For the **L-pro/Gly** system, DFT confirms the presence of two N–H bonds on L-pro, each approximately 1.04 Å in length. These hydrogens engage in strong interactions: one with the $–COO^-$ oxygen within the proline skeleton and the other with a Gly-OH oxygen, consistent with the blue regions observed in the NCI plot (Fig. 3a). The corresponding hydrogen-bond distances range from 1.6 to 1.8 Å.

In the **L-pro/GA** system, similar hydrogen-bonding patterns are observed, with an additional close contact between the $–COO^-$ group of proline and the carboxylic –OH of GA,

© The authors
https://doi.org/10.1007/s40820-026-02358-7

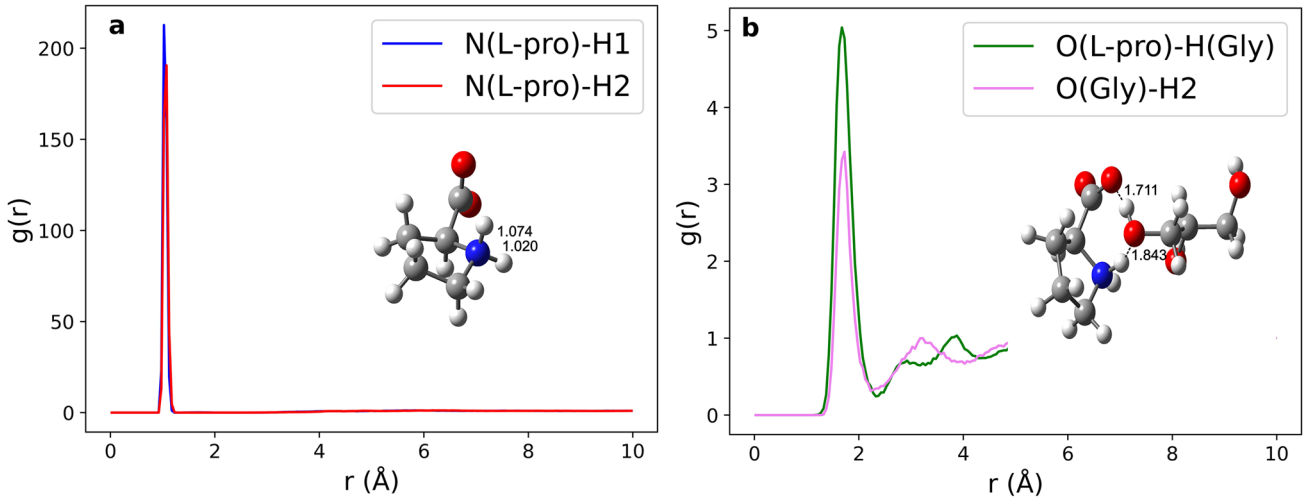


Fig. 1 RDFs showing **a** intramolecular interactions in proline and **b** interactions between L-pro and Gly. Representative relaxed fragments are also reported. Atoms are coloured as follows: carbon in silver, hydrogen in white, oxygen in red, nitrogen in blue

highlighted by the green circle in Fig. 3b. This interaction underscores the stronger directional hydrogen bonding and the more compact network imposed by the extra carbonyl functionality, suggesting enhanced stabilization that may facilitate proton-tunneling pathways.

We further analysed the MD trajectories to probe the dynamic evolution of hydrogen-bonding networks over the course of the simulation, using established geometric criteria commonly applied in the literature: the distance between O(donor) and O(acceptor) $\leq$ 3.5 Å and the O(acceptor) H(donor) O(donor) angle $\geq$ 150° [86] Across all systems, the average number of H-bonds between the HBA and HBD normalized per L-pro unit remains largely constant, reflecting the formation of stable supramolecular architectures. Notably, although the **L-pro/Gly** system exhibits the highest total average number of hydrogen bonds (1.87), compared with **L-pro/GA** (1.33), **L-pro/DEG** (1.40), and **L-pro/BD** (1.21), this metric alone does not fully capture the nature of intermolecular association. In the case of **L-pro/GA**, a substantial contribution arises from partial proton-transfer events mentioned above that are not accounted for in a simple hydrogen-bond count. Specifically, hydrogen atoms originally associated with the HBD are transiently shared with the acceptor, giving rise to interactions that are significantly stronger than conventional hydrogen bonds, as evidenced by the unusually short donor–acceptor distances observed. These results highlight that the strength of association is governed not only by the number of hydrogen

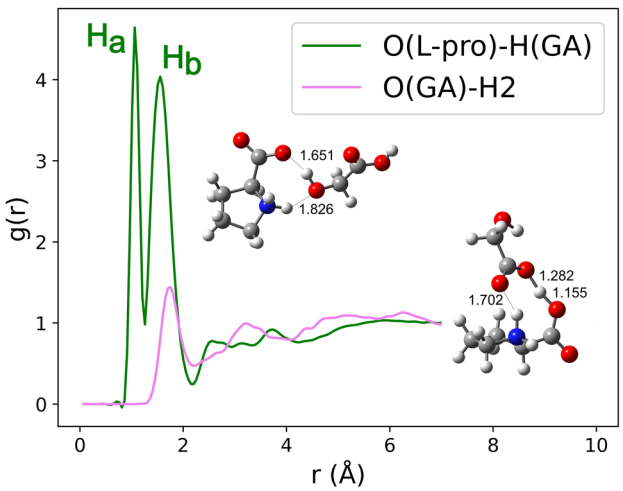


Fig. 2 RDFs showing interatomic distances and coordination in DES **L-pro/GA**. Ha and Hb refer to the carboxylic and the alcoholic hydrogen, respectively. Representative fragments are also shown to illustrate the molecular geometry. Atoms are coloured as follows: carbon in silver, hydrogen in white, oxygen in red, nitrogen in blue

bonds but also by their intrinsic strength, in line with the higher association constant calculated for the GA system [79]. In order to better take into account the persistence of these interactions we have calculated also the HBD-HBA bond lifetimes (see Supporting Information). These results show that, despite the lower number of hydrogen bonds, the **L-pro/GA** system exhibits a longer hydrogen-bond lifetime (4.58 ps) for the dominant GA-OH···O-L-pro interaction

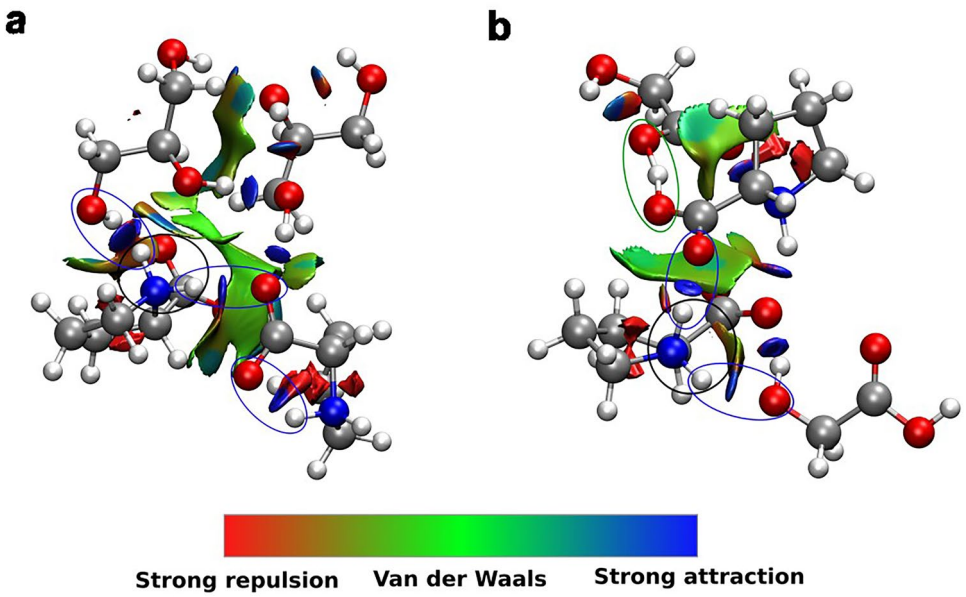


Fig. 3 3D-NCI plot for **a L-pro/Gly** and **b L-pro/GA** generated with an isocontour value of the reduced density gradient set at 0.35. Atoms are coloured as follows: carbon in silver, hydrogen in white, oxygen in red, nitrogen in blue

compared, for example, to Gly-OH··· O-L-pro (3.03 ps) in **L-pro/Gly**. This indicates that the hydrogen bonds formed in the presence of GA are more persistent and dynamically stable, generating a more enduring hydrogen-bond network around the proline oxygen sites. Such enhanced persistence plays a significant role in modulating the local environment and influencing the catalytic behaviour of the system.

Importantly, these structural features correlate with the experimental catalytic activity observed in the Michael addition reaction upon changing the nature of the hydrogen-bond donor. Strongly interacting HBDs, such as GA, stabilize persistent hydrogen bonds that impede proton back-transfer from the amine to the carboxylate, hindering enamine formation (i.e., conversion= 15% with **L-pro/GA**). In contrast, HBDs like Gly, DEG, and BD establish more balanced and dynamic hydrogen-bond networks, preserving molecular flexibility around the reactive centre and enabling higher conversions.

To further assess the robustness of these findings, we extended the analysis to the L-proline/p-toluenesulfonic acid (**L-pro/pTSA**) system, which has been reported to exhibit very low conversion (ca. 5%) in the same ketone Michael addition reaction, significantly lower than that observed for the **L-pro/GA** system [79]. The corresponding RDF analysis (Fig. S1), together with the 11.76 ps lifetime of the pTSA-OH···O-L-pro interaction (Table S13), clearly demonstrates a greater propensity for proton transfer from the HBD to L-proline than in the GA-based system. Consequently, the carboxylate oxygen becomes extensively protonated, significantly reducing the availability of the catalytically active nitrogen functionality.

Intrigued by these observations, we next examined how the nature of the HBD influences the stereoselectivity of the reaction. Notably, literature reports indicate that among the HBDs investigated, only GA affords a high enantiomeric excess, in contrast to the trend observed for catalytic activity.

The enamine, formed by condensation of the catalytic L-proline with the ketone and responsible for generating the stereocentres, represents the key intermediate in the reaction. We therefore extended our ML-MD simulations to systems containing the DES mixture with L-proline in its enamine form and *trans*-β-nitrostyrene. This approach provides direct, atomistic insight into the enamine–nitrostyrene interactions that govern stereocontrol for each of the four HBDs studied, establishing a predictive framework for rationalizing and designing cDESs with tailored enantioselectivity.

As illustrated in Figs. 4a and S4, only the GA-containing system exhibits a markedly strong interaction between the enamine and the substrate (H-bonds = 0.64), in stark contrast to the other three systems, which display only weak

© The authors https://doi.org/10.1007/s40820-026-02358-7

interactions with H-bond values of 0.08, 0.05, and 0.04 for Gly, BD, and DEG, respectively. Conversely, these three systems show significantly stronger interactions between the enamine and the HBD with H-bond values of 0.60, 0.56, and 0.46 for Gly, BD, and DEG, respectively, whereas the GA system exhibits a minimal H-bond value of 0.08.

Although derived from a limited number of data points, these results correlate with the experimentally observed enantiomeric excesses (see Fig. 4b): the GA-based DES delivers high *ee*, whereas Gly, BD, and DEG afford low or negligible selectivity (*ee*(*syn*/*anti*) = rac/rac, 13/rac, and 26/rac, respectively). The data corroborate the cooperative mechanism described in the literature [87–89], in which stereochemical induction is governed by interactions between the proline –COOH and the substrate's nitro group, with these interactions being weakened or rarely observed in the less selective systems.

Furthermore, our data establish a specific threshold for stereocontrol: a minimum of approximately 0.60 enamine–substrate hydrogen bonds is required to impose the geometry-defining contacts necessary for high enantioselectivity. Systems falling below this threshold (e.g., Gly, BD, and DEG at 0.04-0.08) are predicted to afford poor selectivity due to the prevalence of competing enamine–HBD interactions.

Overall, these findings offer an indirect yet compelling rationale for the observed selectivities and provide guidance for the design and optimization of catalyst structures aimed at improving both activity and enantioselectivity. Importantly, the calculated numerical values should be regarded as a system-dependent result of the present dataset rather than a universal threshold, whereas the broader framework based on the balance between enamine–substrate and enamine–HBD hydrogen-bond interactions within the lability window concept provides a general qualitative descriptor for rationalizing stereocontrol trends across related systems.

The mechanistic insights emerging from these observations are illustrated in Fig. 5, highlighting the key interactions and critical steps that influence the selectivity of the process.

3.2 Chiral Quaternary Ammonium Salt-Based DESs

More recently, cDESs based on quaternary ammonium salts have been developed and successfully applied to the Michael addition reaction. Although these systems are composed of molecules that require synthetic preparation, with the associated environmental considerations, they serve as valuable model systems for investigating and understanding the catalytic mechanisms of cDESs.

In these systems, the positive charge resides on a nitrogen atom that is intrinsically quaternary and chemically distinct from the tertiary nitrogen of L-proline. Moreover, the proline-derived cationic scaffold lacks acidic functionalities capable of promoting proton transfer. As a result, these DESs provide a well-defined platform to isolate the effects of a permanently charged HBA, enabling a direct assessment of how a fixed cationic centre, rather than proton-transfer-induced quaternization, governs hydrogen-bonding patterns, intermolecular organization, and ultimately catalytic efficiency.

Consistent with the previous systems, the microstructure was analysed by computing RDFs along the ML-MD trajectories, providing insight into the dominant intermolecular interactions and dynamic organization of the system. In the **1/Gly** DES, a dominant cation-HBD interaction involves the hydroxyl hydrogens of glycerol and the nitrogen of the L-proline, as evidenced by a sharp RDF peak at 1.72 Å (Fig. 6, blue curve), indicative of a strong, directional hydrogen bond.

Analysis of the Br^- anion environment reveals a preferential interaction with the hydroxyl hydrogens of glycerol, giving rise to an intense peak at 2.28 Å (Fig. 6, red curve), whereas contacts with H1 are markedly weaker (2.49 Å, g(r) < 4; black curve). In addition, a broader feature centred at 4.31 Å (Fig. 6, green curve) reflects longer-range electrostatic association between Br^- and the quaternary ammonium centre, consistent with a spatially extended ion-pairing motif in the liquid phase.

In the **2/EG** system, the HBA contains an additional hydroxyl group that promotes the formation of a more extended and interconnected hydrogen-bond network. RDF analysis shows that nitrogen of L-proline engages in hydrogen bonding with the hydroxyl proton (H2) at 1.92 Å (g(r) ≈ 3, pink curve in Fig. 7a), corresponding to a slightly stronger interaction than those involving the ethylene glycol hydrogens (blue curve in Fig. 7a). In addition, the oxygen atoms of EG display a markedly higher propensity to interact with H2 (1.72 Å, g(r) ≈ 3.5, grey curve in Fig. 7a) than with H1 (g(r) ≈ 1.5, brown curve in Fig. 7a), revealing a pronounced asymmetry in the local

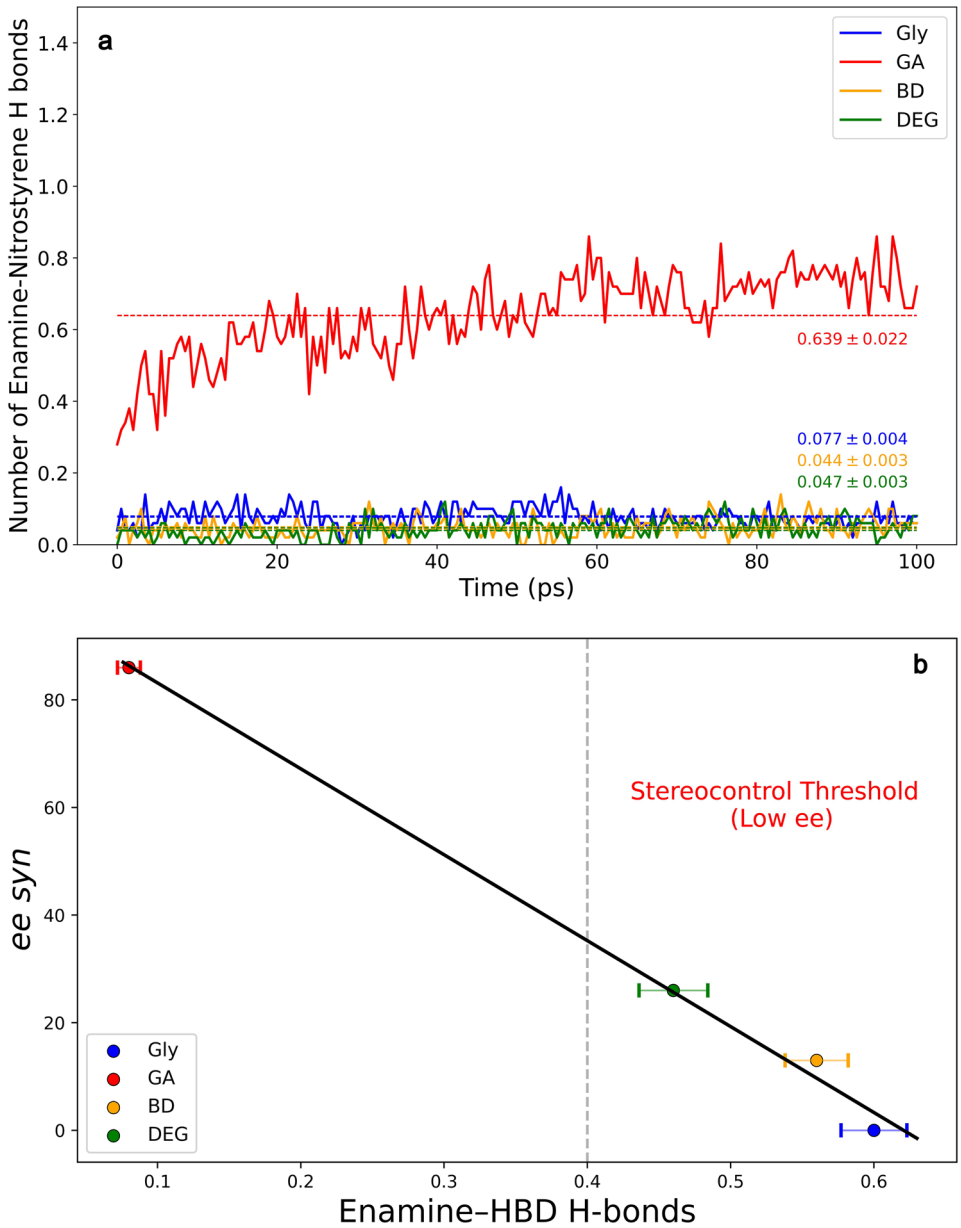


Fig. 4 **a** Time evolution of enamine–nitrostyrene H-bonds for the four HBDs, normalized per L-proline unit, illustrating the hydrogen-bond lability window, with the ~0.60 average enamine–substrate H-bond value defining a high level of stereocontrol. **b** Correlation between *syn*-product ee and average enamine–HBD H-bonds, also reflecting the lability window behaviour, with the low threshold associated with high enantioselectivity. The combination of these limits defines the stereocontrol window separating low and high *ee* regimes

hydrogen-bonding environment between the HBD and HBA moieties. The bromide anion preferentially engages in hydrogen-bonding interactions with the hydroxyl protons of EG and with H2, exhibiting interaction intensities roughly twice those observed for contacts with H1 or with the quaternary nitrogen centre (Fig. 7b). This behaviour underscores the dominant role of the HBD hydroxyl groups and the asymmetric cationic environment in defining the anion-coordination landscape.

In the **3/Urea** DES, cation–HBD interactions are markedly attenuated compared to the polyol-based systems. Consistently, the RDF for the L-proline N–H(urea) pair remains below unity, indicating that direct hydrogen bonding between these sites is only marginally populated. Instead,

© The authors https://doi.org/10.1007/s40820-026-02358-7

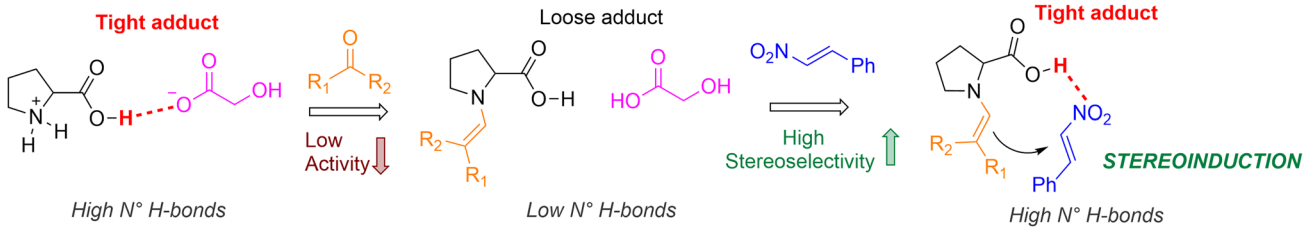


Fig. 5 Mechanistic framework for asymmetric catalysis in cDESs. **Left** Persistent networks cage the active site, hindering enamine formation and turnover. **Centre** High conversion is enabled within a "lability window" that ensures catalyst accessibility. **Right** High enantioselectivity depends on reaching a stereocontrol threshold, where a productive tight adduct establishes the geometry-defining contacts necessary for stereoinduction

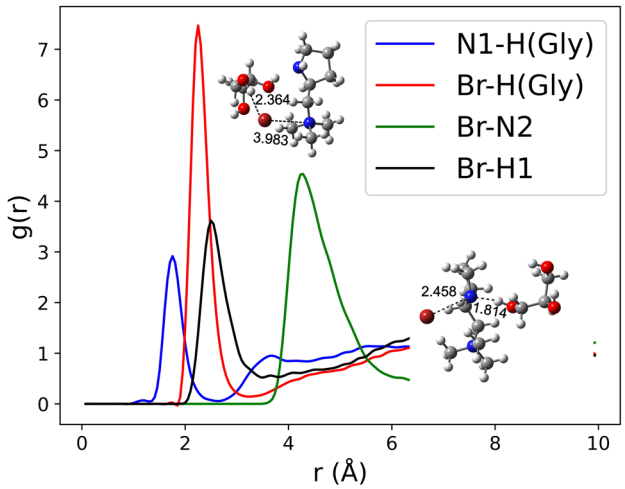


Fig. 6 RDFs showing interatomic distances and coordination in DES **1/Gly**. Representative fragments are also shown to illustrate the molecular geometry. Atoms are coloured as follows: carbon in silver, hydrogen in white, oxygen in red, nitrogen in blue, bromine in dark red

the dominant cation–HBD interaction involves H1 and the carbonyl oxygen of urea, giving rise to a distinct peak at 2.00 Å (Fig. 8a).

Analysis of the Br^- RDFs (Fig. 8b) reveals preferential hydrogen-bonding interactions with the $–NH_2$ protons of urea and with H1, characterized by maxima at ca. 2.5 Å and g(r) values in the 4–5 range. In addition, a broader feature centred at 4.28 Å (green curve) reflects a longer-range electrostatic association between the bromide anion and the quaternary ammonium centre, as already observed for the other systems.

DFT optimizations and NCI analyses were then carried out following the same protocol adopted for the previous systems (Figs. 9 and S37).

For the **1/Gly** system, a short contact of ca. 1.8 Å is found between the hydrogen on the nitrogen atom of the HBA and the oxygen atoms of glycerol, fully consistent with the RDF profiles and visualized by the intense blue isosurfaces in the NCI plot (Fig. 9a). In addition, both the hydroxyl protons of the HBD and H1 engage in hydrogen bonding with the Br^- anion, with characteristic distances in the 2.3–2.4 Å range (blue spots in Fig. 9a)

The **2/EG** system displays a closely related hydrogen-bonding motif, with the main distinction being the presence of short intramolecular hydrogen bonds within the HBA framework at approximately 1.7 Å (see blue spot in Fig. 9b). These interactions slightly rigidify the cationic scaffold while preserving the overall intermolecular organization observed for **1/Gly**.

A markedly different scenario emerges for the **3/Urea** DES. Here, the interaction landscape is dominated by strong urea–urea self-association, with robust hydrogen bonds (1.8–2.0 Å) formed between carbonyl oxygen atoms and amide $–NH_2$ hydrogens, as highlighted by the intense blue regions in Fig. 9c. This extensive HBD self-assembly promotes a folded conformation of the HBA cation, stabilized by hydrogen bonds between the quaternary nitrogen and hydrogens on the carbon skeleton.

Beyond these directional hydrogen bonds, the NCI analyses also reveal diffuse green regions associated with van der Waals contacts among the DES components, underscoring their cooperative role in stabilizing the supramolecular adducts.

The temporal evolution of HBA–HBD hydrogen bonds (Figs. 10 and S10) highlights pronounced differences in interaction strength across the three DESs. The **1/Gly** system exhibits the highest average H-bond count (0.37), whereas

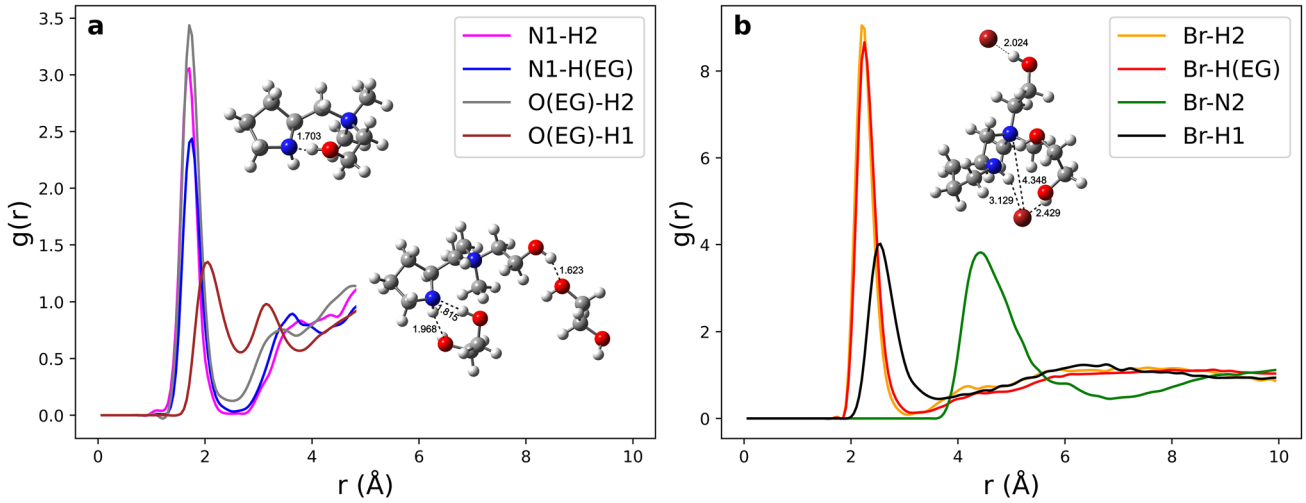


Fig. 7 RDFs showing **a** interactions between the cation of 2 and EG, and **b** interactions involving Br. Representative fragments are also shown to illustrate the molecular geometry. Atoms are coloured as follows: carbon in silver, hydrogen in white, oxygen in red, nitrogen in blue, bromine in dark red

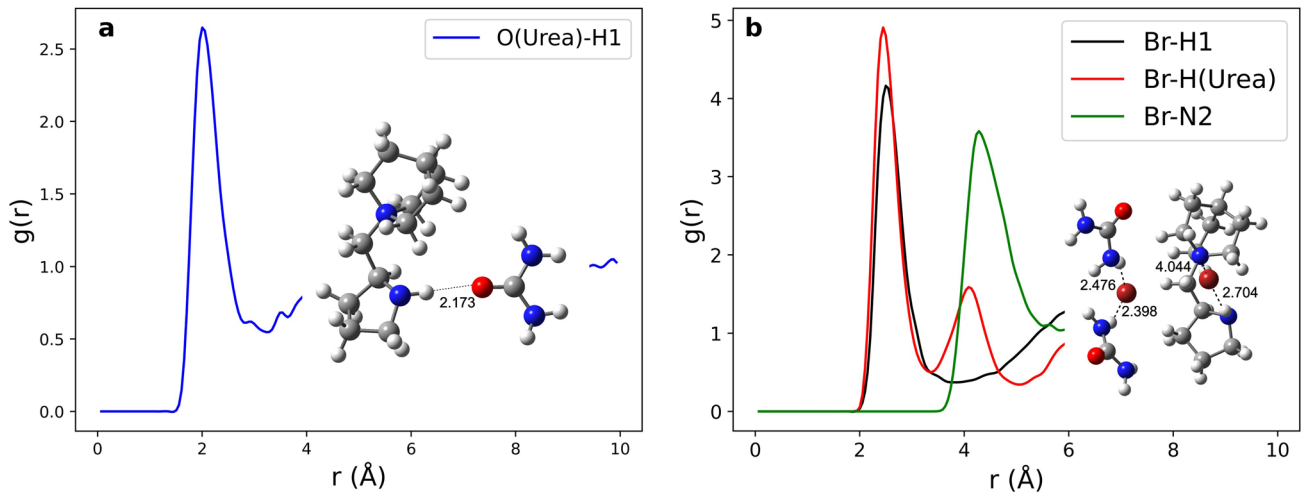


Fig. 8 RDFs showing **a** interactions between the cation of 3 and Urea, and **b** interactions involving Br. Representative fragments are also shown to illustrate the molecular geometry. Atoms are coloured as follows: carbon in silver, hydrogen in white, oxygen in red, nitrogen in blue, bromine in dark red

2/EG and **3/Urea** display substantially weaker interactions, with average values of 0.15 and 0.11, respectively.

This is also consistent with the stronger self-interactions of the HBA skeleton observed for **2/EG** and **3/Urea**, as mentioned above.

Strikingly, this structural trend inversely correlates with the experimentally observed catalytic performance: DESs with weaker or more labile HBA–HBD networks (**2/EG** and **3/Urea**) achieve higher conversion, whereas **1/Gly**, characterized by the most persistent hydrogen-bonding network, shows the lowest catalytic efficiency.

This low efficiency in **1/Gly** (17% conversion) is a direct consequence of the sequestration of the active site within a static hydrogen-bond cage. Atomistic analysis reveals that the nucleophilic nitrogen centre is directly occupied by a strong, directional hydrogen bond with the glycerol hydroxyl groups (1.72 Å), which is further stabilized by

© The authors https://doi.org/10.1007/s40820-026-02358-7

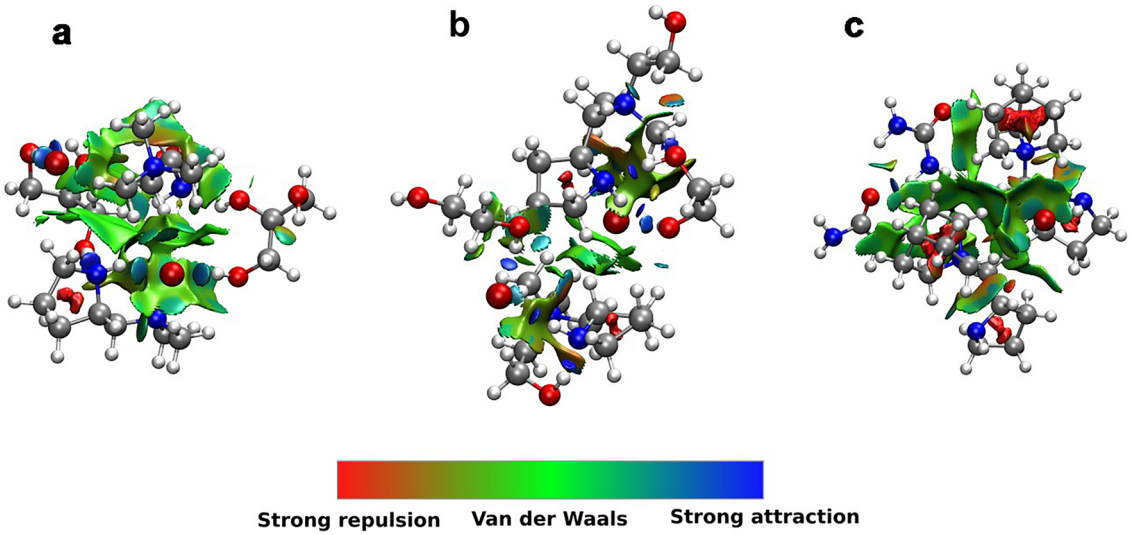


Fig. 9 3D-NCI plot for **a 1/Gly**, **b 2/EG,** and **c 3/Urea** generated with an isocontour value of the reduced density gradient set at 0.35. Atoms are coloured as follows: carbon in silver, hydrogen in white, oxygen in red, nitrogen in blue, bromine in dark red

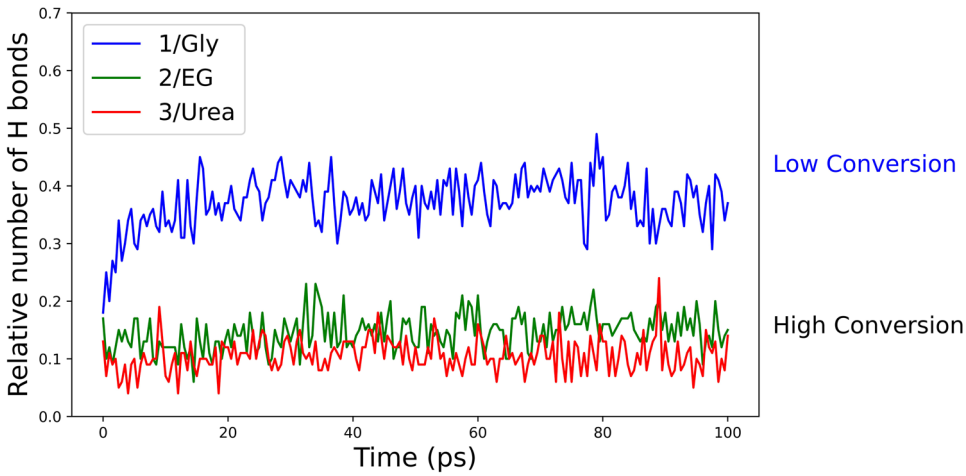


Fig. 10 Time evolution of HBA–HBD hydrogen bonds normalized per HBA unit. The analysis reveals distinct dynamic regimes, ranging from labile hydrogen-bond networks to highly persistent supramolecular assemblies, which underpin the observed differences in catalytic turnover across the investigated cDESs

the bromide anion. This anion acts as a supramolecular anchor, engaging in simultaneous interactions with both the HBD (2.28 Å) and the HBA (2.49 Å), effectively locking the catalyst in a rigid coordination environment.

The resulting physical and electronic barrier in **1/Gly**, quantified by the highest average H-bond count of 0.37, blocks the ketone substrate's approach, making the initial nucleophilic attack required for enamine formation energetically unfavourable. In contrast, the near-quantitative conversions of **2/EG** and **3/Urea** are facilitated by their ability to avoid such sequestration. In **2/EG**, the HBA's coordination potential is satisfied through internal hydrogen bonds (~1.7 Å), which limit its reliance on the external solvent network. Similarly, in the **3/Urea** system, the urea molecules exhibit strong self-association (1.8–2.0 Å), effectively 'ignoring' the catalyst and leaving the nitrogen centre accessible for substrate activation.

This behaviour suggests that, as observed for the L-proline-based cDESs discussed above, efficient catalysis in quaternary ammonium-based DESs also relies on an optimal balance between hydrogen-bond strength and molecular mobility. Excessively strong HBA–HBD interactions impede enamine formation, whereas more labile hydrogen bonds maintain local flexibility, promoting substrate activation and product formation. Crucially, in these systems, the nitrogen atom involved in enamine formation remains unquaternized, preserving its nucleophilicity and further enhancing catalytic efficiency.

By integrating these observations, tentative quantitative benchmarks for the rational design of cDESs within the present set of systems can be proposed. Specifically, average HBA–HBD hydrogen-bond counts close to 0.1 (as observed for **2/EG** and **3/Urea**), delineate a "lability window" that enables efficient substrate access and is predictive of near-quantitative catalytic conversion in the systems examined here. In contrast, systems characterized by average hydrogen-bond counts exceeding 0.30 (as exemplified by **1/Gly**) form persistent supramolecular cages that sequester the active site and severely limit turnover.

An additional analysis examining the relationship between enamine–HBD hydrogen-bond interactions and the experimentally observed diastereomeric excess is provided in the Supporting Information (Table S7). The observed trend is consistent with the conclusions drawn for the systems analysed in the preceding section and further supports the relevance of this descriptor across the systems investigated.

Establishing these numerical thresholds enhances the ML-MD framework by providing a more quantitative basis for the interpretation of DES behaviour and supports its use as a promising tool for the a priori screening of the large combinatorial space of DES components.

The final step was to assess the transferability of the proposed framework to a different organocatalytic transformation. To this end, we extended the same protocol to a Michael addition/aldol-type reaction between cyclohexanone and 3-nitrobenzaldehyde, recently reported for a series of L-proline-based cDESs [90]. Applying the hydrogen-bond and structural descriptors developed in this work, we observed a clear and consistent correlation between the enamine–HBD hydrogen-bond network and the enantioselectivity of the *anti*-product across the systems investigated under experimentally comparable conditions (Fig. S2).

These results further support the broader applicability of the proposed descriptors and reinforce their potential as practical tools for the rational design and screening of catalytic cDES systems.

4 Conclusions

This work establishes ML-MD as a transformative, resource-efficient approach for dissecting and predicting the function of complex catalytic solvents.

Importantly, the ability to establish transferable structure–property relationships without re-deriving system-specific force fields for each new DES represents a key advantage of the ML-MD approach. In contrast to classical workflows, which require repeated parametrization, force-field development, and validation for every new DES composition, ML-MD leverages a pre-trained machine-learning potential to directly sample the relevant configurational space with near ab initio accuracy. This capability enables the rapid characterization of the hydrogen-bonding patterns, supramolecular organization, and dynamic interactions that govern catalytic performance across chemically distinct DES formulations, without the need for system-specific model development. This aspect is particularly relevant for DES systems, whose vast and continuously expanding compositional space can be explored by varying the HBA ratio and the chemical nature of the constituent components. Given the growing number of DES formulations reported in the literature, often encompassing diverse and rapidly evolving chemistries, the ability to efficiently screen and compare different compositions makes it possible to move beyond empirical optimization towards the rational design of multifunctional catalytic media.

To the best of our knowledge, this represents the first study to apply a fully dynamic, molecularly resolved computational framework to elucidate the role of DESs in asymmetric catalysis. By moving beyond static structural descriptions and explicitly resolving the dynamics of hydrogen-bond networks in cDESs, this framework decodes the molecular origins of experimentally observed reactivity and stereoselectivity. For protic cDESs based on L-proline, catalytic activity is inherently limited by intramolecular proton transfer to the amine, which generates a quaternary N^+ centre and attenuates nucleophilicity. The hydrogen-bond donor critically modulates this scaffold: strongly associating

© The authors https://doi.org/10.1007/s40820-026-02358-7

donors (e.g., glycolic acid) lock the protonated state within a rigid, persistent network, suppressing activity. Conversely, more dynamic HBDs (e.g., glycerol and diols) preserve the molecular flexibility required for efficient catalytic turnover. With respect to stereoselectivity, weak and transient interactions between the HBD and the key enamine intermediate favour its engagement with the nitrostyrene substrate, thereby enabling a stereoselective reaction pathway.

In contrast, for pre-quaternized ammonium-based cDESs where the catalytic amine remains unprotonated, performance relies entirely on the solvent's supramolecular architecture. Here, efficient catalysis correlates with weaker, more labile HBA–HBD interactions, which prevent the sequestration of the nucleophilic active site within a persistent supramolecular cage. This 'cage effect' serves as a primary physical barrier to substrate activation, a finding that applies across both protic and pre-quaternized cDES families. By defining these boundaries, our framework provides a concrete set of design rules that move cDES development from empirical trial-and-error towards quantitative, knowledge-driven discovery. The ability to correlate quantitative descriptors of hydrogen-bond network lability with experimental conversion and enantiomeric excess represents a significant advance. By providing a predictive, microscopically informed description of how DES structure governs catalytic function, this strategy transcends the specific Michael addition case study, providing a general computational roadmap for navigating the vast combinatorial space of hydrogen-bond acceptor and donor pairings, accelerating the discovery of chiral eutectic solvents with tailored catalytic properties.

Importantly, these descriptors can provide physically meaningful input features for high-throughput virtual screening workflows, enabling a more rapid evaluation and ranking of candidate DES formulations before experimental testing. Furthermore, their integration with experimental observables within hybrid machine-learning models can offer a direct route towards predictive frameworks that bridge molecular-level simulations with macroscopic catalytic performance.

Ultimately, this work elevates chiral deep eutectic solvents from passive green media to rationally designable, multifunctional catalytic systems, bridging molecular-level simulation with the practical demands of sustainable chemical transformations.

Acknowledgments D.A.A. thanks Spanish Ministry of Science, Innovation and Universities (project PID2021-126445OB-I00) and University of Alicante (VIGROB-173). Laura Falivene thanks Italian Ministry of University and Research (PRIN 2022, CUP E53D23008360006). Luca Fortunato acknowledges support from the European Research Council (ERC) Project AMF (Grant No. 101163880).

Author contributions Michele Tomasini: Data curation, Validation, Software, Investigation, Methodology. Matteo Tiecco: Conceptualization, Writing. Diego A. Alonso: Validation, Writing. Luca Fortunato: Conceptualization, Validation, Writing—review and editing. Laura Falivene: Visualization, Supervision, Project administration, Validation, Data curation, Conceptualization, Writing—review and editing.

Declarations

Conflict of interest The authors declare no conflict of interest. They have no known conflict of financial interest or personal relationships that could have appeared to influence the work reported in this paper.

Open Access This article is licensed under a Creative Commons Attribution 4.0 International License, which permits use, sharing, adaptation, distribution and reproduction in any medium or format, as long as you give appropriate credit to the original author(s) and the source, provide a link to the Creative Commons licence, and indicate if changes were made. The images or other third party material in this article are included in the article's Creative Commons licence, unless indicated otherwise in a credit line to the material. If material is not included in the article's Creative Commons licence and your intended use is not permitted by statutory regulation or exceeds the permitted use, you will need to obtain permission directly from the copyright holder. To view a copy of this licence, visit http://creativecommons.org/licenses/by/4.0/.

Supplementary Information The online version contains supplementary material available at https://doi.org/10.1007/s40820-026-02358-7.

References

1. P. Anastas, N. Eghbali, Green chemistry: principles and practice. Chem. Soc. Rev. **39**(1), 301–312 (2010). https://doi.org/10.1039/b918763b
2. B.B. Hansen, S. Spittle, B. Chen, D. Poe, Y. Zhang et al., Deep eutectic solvents: a review of fundamentals and applications. Chem. Rev. **121**(3), 1232–1285 (2021). https://doi.org/10.1021/acs.chemrev.0c00385
3. Q. Zhang, K. De Oliveira Vigier, S. Royer, F. Jérôme, Deep eutectic solvents: syntheses, properties and applications. Chem. Soc. Rev. **41**(21), 7108–7146 (2012). https://doi.org/10.1039/c2cs35178a

4. A. Zobeid, F. Abbasi, S. Azadi, Deep eutectic solvents: a review of syntheses, properties, and their applications in different fields. Adv. Appl. NanoBio. Technol. **6**(2), 1–45 (2025). https://doi.org/10.18502/aanbt.v6i2.18615
5. T. Sun, S. Zheng, H. Du, Z. Tao, Synergistic effect of cation and anion for low-temperature aqueous zinc-ion battery. Nano-Micro Lett. **13**(1), 204 (2021). https://doi.org/10.1007/s40820-021-00733-0
6. A.E. Ünlü, A. Arıkaya, S. Takaç, Use of deep eutectic solvents as catalyst: a mini-review. Green Process. Synth. **8**(1), 355–372 (2019). https://doi.org/10.1515/gps-2019-0003
7. T. Zhang, T. Doert, H. Wang, S. Zhang, M. Ruck, Inorganic synthesis based on reactions of ionic liquids and deep eutectic solvents. Angew. Chem. Int. Ed. **60**(41), 22148–22165 (2021). https://doi.org/10.1002/anie.202104035
8. R. Umapathi, S.M. Ghoreishian, K. Kumar, D. Dhiman, G.M. Rani et al., Deep eutectic solvents induced changes in the phase transition behavior of smart polymers: a sustainable future approach. Phys. Chem. Chem. Phys. **25**(32), 21131–21148 (2023). https://doi.org/10.1039/d3cp01913f
9. R. Umapathi, K. Kumar, S.M. Ghoreishian, G.M. Rani, Y.S. Huh et al., Interactions between a biomedical thermoresponsive polymer and imidazolium-based ionic liquids: a comprehensive biophysical investigation. Colloids Surf. A Physicochem. Eng. Aspects **641**, 128619 (2022). https://doi.org/10.1016/j.colsurfa.2022.128619
10. R. Umapathi, K. Kumar, S.M. Ghoreishian, G.M. Rani, S.Y. Park et al., Tunnelling the structural insights between poly(N-isopropylacrylamide) and imidazolium sulfate ionic liquids. J. Mol. Liq. **360**, 119404 (2022). https://doi.org/10.1016/j.molliq.2022.119404
11. R. Umapathi, K. Kumar, S.M. Ghoreishian, G.M. Rani, S.Y. Park et al., Effect of imidazolium nitrate ionic liquids on conformational changes of poly(*N*-vinylcaprolactam). ACS Omega **7**(44), 39742–39749 (2022). https://doi.org/10.1021/acsomega.2c03650
12. K. Kumar, R. Umapathi, S. Mor, S.M. Ghoreishian, J.N. Tiwari et al., Manipulation of thermoresponsive polymers using biomolecules. ACS Appl. Polym. Mater. **5**(5), 3181–3200 (2023). https://doi.org/10.1021/acsapm.2c02162
13. A.J. Burke, E.P. Carreiro, H.-J. Federsel, How deep eutectic solvents are currently shaping organocatalytic and enzymatic asymmetric catalysis. RSC Sustain. **3**(9), 3883–3890 (2025). https://doi.org/10.1039/d5su00265f
14. G. Cainelli, P. Galletti, D. Giacomini, Solvent effects on stereoselectivity: more than just an environment. Chem. Soc. Rev. **38**(4), 990 (2009). https://doi.org/10.1039/b802815j
15. D.A. Alonso, S.-J. Burlingham, R. Chinchilla, G. Guillena, D.J. Ramón et al., Asymmetric organocatalysis in deep eutectic solvents. Eur. J. Org. Chem. **29**, 4065–4071 (2021). https://doi.org/10.1002/ejoc.202100385
16. S.J. Burlingham, J.A. Ñíguez, F.J. Sierra-Molero, A. Torregrosa-Chinillach, A. Baeza et al., Chiral ionic liquids and deep eutectic solvents. in *Enantioselective Organocatalysis*, ed. by P.I. Dalko. (Wiley-VCH, Weinheim, 2026), pp. 1461–1486. https://doi.org/10.1002/9783527845552.ch39
17. I.I.I. Alkhatib, D. Bahamon, F. Llovell, M.R.M. Abu-Zahra, L.F. Vega, Perspectives and guidelines on thermodynamic modelling of deep eutectic solvents. J. Mol. Liq. **298**, 112183 (2020). https://doi.org/10.1016/j.molliq.2019.112183
18. D.V. Wagle, L. Adhikari, G.A. Baker, Computational perspectives on structure, dynamics, gas sorption, and bio-interactions in deep eutectic solvents. Fluid Phase Equilib. **448**, 50–58 (2017). https://doi.org/10.1016/j.fluid.2017.04.018
19. H. Sun, Y. Li, X. Wu, G. Li, Theoretical study on the structures and properties of mixtures of urea and choline chloride. J. Mol. Model. **19**(6), 2433–2441 (2013). https://doi.org/10.1007/s00894-013-1791-2
20. S.L. Perkins, P. Painter, C.M. Colina, Molecular dynamic simulations and vibrational analysis of an ionic liquid analogue. J. Phys. Chem. B **117**(35), 10250–10260 (2013). https://doi.org/10.1021/jp404619x
21. S.L. Perkins, P. Painter, C.M. Colina, Experimental and computational studies of choline chloride-based deep eutectic solvents. J. Chem. Eng. Data **59**(11), 3652–3662 (2014). https://doi.org/10.1021/je500520h
22. V. Migliorati, F. Sessa, P. D'Angelo, Deep eutectic solvents: a structural point of view on the role of the cation. Chem. Phys. Lett. **737**, 100001 (2019). https://doi.org/10.1016/j.cpletx.2018.100001
23. D. Tolmachev, N. Lukasheva, R. Ramazanov, V. Nazarychev, N. Borzdun et al., Computer simulations of deep eutectic solvents: challenges, solutions, and perspectives. Int. J. Mol. Sci. **23**(2), 645 (2022). https://doi.org/10.3390/ijms23020645
24. S. Kaur, A. Malik, H.K. Kashyap, Anatomy of microscopic structure of ethaline deep eutectic solvent decoded through molecular dynamics simulations. J. Phys. Chem. B **123**(39), 8291–8299 (2019). https://doi.org/10.1021/acs.jpcb.9b06624
25. D. Chen, R. Lu, R. Yu, H. Zhao, D. Wu et al., Tuning active metal atomic spacing by filling of light atoms and resulting reversed hydrogen adsorption-distance relationship for efficient catalysis. Nano-Micro Lett. **15**(1), 168 (2023). https://doi.org/10.1007/s40820-023-01142-1
26. C. Velez, O. Acevedo, Simulation of deep eutectic solvents: progress to promises. WIREs Comput. Mol. Sci. **12**(4), e1598 (2022). https://doi.org/10.1002/wcms.1598
27. B. Doherty, O. Acevedo, OPLS force field for choline chloride-based deep eutectic solvents. J. Phys. Chem. B **122**(43), 9982–9993 (2018). https://doi.org/10.1021/acs.jpcb.8b06647
28. X. Zhong, C. Velez, O. Acevedo, Partial charges optimized by genetic algorithms for deep eutectic solvent simulations. J. Chem. Theory Comput. **17**(5), 3078–3087 (2021). https://doi.org/10.1021/acs.jctc.1c00047
29. J.P. Bittner, L. Huang, N. Zhang, S. Kara, S. Jakobtorweihen, Comparison and validation of force fields for deep eutectic solvents in combination with water and alcohol dehydrogenase. J. Chem. Theory Comput. **17**(8), 5322–5341 (2021). https://doi.org/10.1021/acs.jctc.1c00274
30. K. Goloviznina, Z. Gong, A.A.H. Padua, The CL&Pol polarizable force field for the simulation of ionic liquids and eutectic

© The authors https://doi.org/10.1007/s40820-026-02358-7

solvents. WIREs Comput. Mol. Sci. **12**(3), e1572 (2022). https://doi.org/10.1002/wcms.1572

31. K.-J. Jeong, J.G. McDaniel, A. Yethiraj, Deep eutectic solvents: molecular simulations with a first-principles polarizable force field. J. Phys. Chem. B **125**(26), 7177–7186 (2021). https://doi.org/10.1021/acs.jpcb.1c01692
32. X. Bai, X. Zhang, Artificial intelligence-powered materials science. Nano-Micro Lett. **17**(1), 135 (2025). https://doi.org/10.1007/s40820-024-01634-8
33. Y. Cao, H. Fu, J. Lu, Y. Chen, T. Jing et al., Artificial intelligence empowered new materials: discovery, synthesis, prediction to validation. Nano-Micro Lett. **18**(1), 109 (2026). https://doi.org/10.1007/s40820-025-01945-4
34. S. Wang, J. Liu, X. Song, H. Xu, Y. Gu et al., Artificial intelligence empowers solid-state batteries for material screening and performance evaluation. Nano-Micro Lett. **17**(1), 287 (2025). https://doi.org/10.1007/s40820-025-01797-y
35. J.P. Reid, M.S. Sigman, Holistic prediction of enantioselectivity in asymmetric catalysis. Nature **571**(7765), 343–348 (2019). https://doi.org/10.1038/s41586-019-1384-z
36. S.-W. Li, L.-C. Xu, C. Zhang, S.-Q. Zhang, X. Hong, Reaction performance prediction with an extrapolative and interpretable graph model based on chemical knowledge. Nat. Commun. **14**(1), 3569 (2023). https://doi.org/10.1038/s41467-023-39283-x
37. L. Cheng, P.-L. Shao, J. Lv, H. Xiao, Y. Sun et al., Chemistry-informed deep learning model for predicting stereoselectivity and absolute configuration in asymmetric hydrogenation. Nat. Comput. Sci. **6**(2), 145–155 (2026). https://doi.org/10.1038/s43588-025-00920-8
38. T.T. Duignan, The potential of neural network potentials. ACS Phys. Chem. Au **4**(3), 232–241 (2024). https://doi.org/10.1021/acsphyschemau.4c00004
39. O.T. Unke, S. Chmiela, H.E. Sauceda, M. Gastegger, I. Poltavsky et al., Machine learning force fields. Chem. Rev. **121**(16), 10142–10186 (2021). https://doi.org/10.1021/acs.chemrev.0c01111
40. J. Behler, M. Parrinello, Generalized neural-network representation of high-dimensional potential-energy surfaces. Phys. Rev. Lett. **98**(14), 146401 (2007). https://doi.org/10.1103/PhysRevLett.98.146401
41. O.T. Unke, M. Meuwly, PhysNet: a neural network for predicting energies, forces, dipole moments, and partial charges. J. Chem. Theory Comput. **15**(6), 3678–3693 (2019). https://doi.org/10.1021/acs.jctc.9b00181
42. M. Kulichenko, B. Nebgen, N. Lubbers et al., Data generation for machine learning interatomic potentials and beyond. Chem. Rev. **124**(24), 13681–13714 (2024). https://doi.org/10.1021/acs.chemrev.4c00572
43. O. Shayestehpour, S. Zahn, Efficient molecular dynamics simulations of deep eutectic solvents with first-principles accuracy using machine learning interatomic potentials. J. Chem. Theory Comput. **19**(23), 8732–8742 (2023). https://doi.org/10.1021/acs.jctc.3c00944
44. R. Galvelis, A. Varela-Rial, S. Doerr, R. Fino, P. Eastman et al., NNP/MM: accelerating molecular dynamics simulations with machine learning potentials and molecular mechanics. J. Chem. Inf. Model. **63**(18), 5701–5708 (2023). https://doi.org/10.1021/acs.jcim.3c00773
45. H. Chan, B. Narayanan, M.J. Cherukara, F.G. Sen, K. Sasikumar et al., Machine learning classical interatomic potentials for molecular dynamics from first-principles training data. J. Phys. Chem. C **123**(12), 6941–6957 (2019). https://doi.org/10.1021/acs.jpcc.8b09917
46. Y.-W. Zhang, V. Sorkin, Z.H. Aitken, A. Politano, J. Behler et al., Roadmap for the development of machine learning-based interatomic potentials. Modell. Simul. Mater. Sci. Eng. **33**(2), 023301 (2025). https://doi.org/10.1088/1361-651x/ad9d63
47. S. Saini, A. Sharma, N. Saini, N. Kaur, N. Singh, Machine learning-driven optimization of deep eutectic solvents: accelerating physicochemical properties modeling. Sustain. Mater. Technol. **45**, e01536 (2025). https://doi.org/10.1016/j.susmat.2025.e01536
48. D. Bedrov, J.-P. Piquemal, O. Borodin, A.D. MacKerell Jr., B. Roux et al., Molecular dynamics simulations of ionic liquids and electrolytes using polarizable force fields. Chem. Rev. **119**(13), 7940–7995 (2019). https://doi.org/10.1021/acs.chemrev.8b00763
49. E.J. Maginn, Molecular simulation of ionic liquids: current status and future opportunities. J. Phys. Condens. Matter **21**(37), 373101 (2009). https://doi.org/10.1088/0953-8984/21/37/373101
50. M. Gődény, T. Nagy, B. Viskolcz, M. Bán, Reactive molecular dynamics simulations of ionic liquids: a review of computational approaches. Liquids **5**(1), 8 (2025). https://doi.org/10.3390/liquids5010008
51. B.L. Bhargava, Molecular dynamics simulations of ionic liquids, in *Theoretical and Computational Approaches to Predicting Ionic Liquid Properties*. (Elsevier, 2021), pp.87–104. https://doi.org/10.1016/b978-0-12-820280-7.00007-3
52. J.N. Lane, V.J. Klimkowski, T.A. Hopkins, Molecular dynamics investigation of deep eutectic solvent structure and properties based on hydrogen bond acceptor variation. J. Mol. Liq. **423**, 127009 (2025). https://doi.org/10.1016/j.molliq.2025.127009
53. C. Fan, Y. Liu, T. Sebbah, X. Cao, A theoretical study on terpene-based natural deep eutectic solvent: relationship between viscosity and hydrogen-bonding interactions. Glob. Chall. **5**(3), 2000103 (2021). https://doi.org/10.1002/gch2.202000103
54. A. Gutiérrez, M. Atilhan, S. Aparicio, Molecular dynamics study on water confinement in deep eutectic solvents. J. Mol. Liq. **339**, 116758 (2021). https://doi.org/10.1016/j.molliq.2021.116758
55. T. Palomba, G. Ciancaleoni, T. Del Giacco, R. Germani, F. Ianni, M. Tiecco, Deep eutectic solvents formed by chiral components as versatile media for asymmetric synthesis. J. Mol. Liq. **262**, 285 (2018). https://doi.org/10.1016/j.molliq.2018.04.096

56. C.R. Ashworth, R.P. Matthews, T. Welton, P.A. Hunt, Doubly ionic hydrogen bond interactions within the choline chloride-urea deep eutectic solvent. Phys. Chem. Chem. Phys. **18**(27), 18145–18160 (2016). https://doi.org/10.1039/c6cp02815b
57. H.S. Salehi, H.M. Polat, F. de Meyer, C. Houriez, C. Coquelet et al., Vapor pressures and vapor phase compositions of choline chloride urea and choline chloride ethylene glycol deep eutectic solvents from molecular simulation. J. Chem. Phys. **155**(11), 114504 (2021). https://doi.org/10.1063/5.0062408
58. A.P. Thompson, H.M. Aktulga, R. Berger, D.S. Bolintineanu, W.M. Brown et al., LAMMPS - a flexible simulation tool for particle-based materials modeling at the atomic, meso, and continuum scales. Comput. Phys. Commun. **271**, 108171 (2022). https://doi.org/10.1016/j.cpc.2021.108171
59. Matlantis, Software-as-a-service materials discovery platform. Preferred Networks, Inc., https://matlantis.com . Accessed 24 February 2026
60. S. Takamoto, C. Shinagawa, D. Motoki, K. Nakago, W. Li et al., Towards universal neural network potential for material discovery applicable to arbitrary combination of 45 elements. Nat. Commun. **13**(1), 2991 (2022). https://doi.org/10.1038/s41467-022-30687-9
61. L. Martínez, R. Andrade, E.G. Birgin, J.M. Martínez, PACKMOL: a package for building initial configurations for molecular dynamics simulations. J. Comput. Chem. **30**(13), 2157–2164 (2009). https://doi.org/10.1002/jcc.21224
62. H.J.C. Berendsen, J.P.M. Postma, W.F. van Gunsteren, A. DiNola, J.R. Haak, Molecular dynamics with coupling to an external bath. J. Chem. Phys. **81**(8), 3684–3690 (1984). https://doi.org/10.1063/1.448118
63. L. Verlet, Computer "experiments" on classical fluids. I. thermodynamical properties of lennard-jones molecules. Phys. Rev. **159**, 98–103 (1967). https://doi.org/10.1103/PhysRev.159.98
64. N. Michaud-Agrawal, E.J. Denning, T.B. Woolf, O. Beckstein, MDAnalysis: a toolkit for the analysis of molecular dynamics simulations. J. Comput. Chem. **32**(10), 2319–2327 (2011). https://doi.org/10.1002/jcc.21787
65. W. Humphrey, A. Dalke, K. Schulten, VMD: visual molecular dynamics. J. Mol. Graph. **14**(1), 33–38 (1996). https://doi.org/10.1016/0263-7855(96)00018-5
66. A. Becke, Density-functional exchange-energy approximation with correct asymptotic behavior. Phys. Rev. A **38**(6), 3098–3100 (1988). https://doi.org/10.1103/physreva.38.3098
67. C. Lee, W. Yang, R. Parr, Development of the *Colle*-Salvetti correlation-energy formula into a functional of the electron density. Phys. Rev. B **37**(2), 785–789 (1988). https://doi.org/10.1103/physrevb.37.785
68. A.D. Becke, A new mixing of Hartree-Fock and local density-functional theories. J. Chem. Phys. **98**(2), 1372–1377 (1993). https://doi.org/10.1063/1.464304
69. S. Grimme, J. Antony, S. Ehrlich, H. Krieg, A consistent and accurate *ab initio* parametrization of density functional dispersion correction (DFT-D) for the 94 elements H-Pu. J. Chem. Phys. **132**(15), 154104 (2010). https://doi.org/10.1063/1.3382344
70. W.J. Hehre, R. Ditchfield, J.A. Pople, Self: consistent molecular orbital methods. XII. Further extensions of Gaussian: type basis sets for use in molecular orbital studies of organic molecules. J. Chem. Phys. **56**(5), 2257–2261 (1972). https://doi.org/10.1063/1.1677527
71. P.C. Hariharan, J.A. Pople, The influence of polarization functions on molecular orbital hydrogenation energies. Theor. Chim. Acta **28**(3), 213–222 (1973). https://doi.org/10.1007/BF00533485
72. R. Krishnan, J.S. Binkley, R. Seeger, J.A. Pople, Self-consistent molecular orbital methods. XX. A basis set for correlated wave functions. J. Chem. Phys. **72**(1), 650–654 (1980). https://doi.org/10.1063/1.438955
73. T. Clark, J. Chandrasekhar, G.W. Spitznagel, P. Von Ragué Schleyer, Efficient diffuse function-augmented basis sets for anion calculations. III. The 3-21+G basis set for first-row elements, Li–F. J. Comput. Chem. **4**(3), 294–301 (1983). https://doi.org/10.1002/jcc.540040303
74. J.-D. Chai, M. Head-Gordon, Long-range corrected hybrid density functionals with damped atom-atom dispersion corrections. Phys. Chem. Chem. Phys. **10**(44), 6615–6620 (2008). https://doi.org/10.1039/b810189b
75. F. Weigend, R. Ahlrichs, Balanced basis sets of split valence, triple *zeta* valence and quadruple *zeta* valence quality for H to Rn: design and assessment of accuracy. Phys. Chem. Chem. Phys. **7**(18), 3297–3305 (2005). https://doi.org/10.1039/b508541a
76. E.R. Johnson, S. Keinan, P. Mori-Sánchez, J. Contreras-García, A.J. Cohen et al., Revealing noncovalent interactions. J. Am. Chem. Soc. **132**(18), 6498–6506 (2010). https://doi.org/10.1021/ja100936w
77. J. Contreras-García, E.R. Johnson, S. Keinan, R. Chaudret, J.-P. Piquemal et al., NCIPLOT: a program for plotting noncovalent interaction regions. J. Chem. Theory Comput. **7**(3), 625–632 (2011). https://doi.org/10.1021/ct100641a
78. T. Lu, F. Chen, Multiwfn: a multifunctional wavefunction analyzer. J. Comput. Chem. **33**(5), 580–592 (2012). https://doi.org/10.1002/jcc.22885
79. M. Tiecco, D.A. Alonso, D.R. Ñíguez, G. Ciancaleoni, G. Guillena et al., Assessment of the organocatalytic activity of chiral L-proline-based deep eutectic solvents based on their structural features. J. Mol. Liq. **313**, 113573 (2020). https://doi.org/10.1016/j.molliq.2020.113573
80. S.J. Burlingham, J.A. Ñíguez, A. Torregrosa-Chinillach, D.R. Ñíguez, R. Chinchilla et al., Synthesis, characterization and organocatalytic activity of novel chiral (ammoniummethyl) pyrrolidine-derived deep eutectic solvents. J. Mol. Liq. **411**, 125724 (2024). https://doi.org/10.1016/j.molliq.2024.125724
81. M.P. Allen, D.J. Tildesley, *Computer Simulation of Liquids*, 2nd ed. (Oxford University Press, Oxford, United Kingdom, 2017)
82. A. van den Bruinhorst, T. Spyriouni, J.-R. Hill, M.C. Kroon, Experimental and molecular modeling evaluation of the physicochemical properties of proline-based deep eutectic solvents.

© The authors https://doi.org/10.1007/s40820-026-02358-7

J. Phys. Chem. B **122**(1), 369–379 (2018). https://doi.org/10.1021/acs.jpcb.7b09540

83. G.A. Cisneros, K.T. Wikfeldt, L. Ojamäe, J. Lu, Y. Xu et al., Modeling molecular interactions in water: from pairwise to many-body potential energy functions. Chem. Rev. **116**(13), 7501–7528 (2016). https://doi.org/10.1021/acs.chemrev.5b00644
84. J. Wang, G. Román-Pérez, J.M. Soler, E. Artacho, M.-V. Fernández-Serra, Density, structure, and dynamics of water: the effect of van der Waals interactions. J. Chem. Phys. **134**(2), 024516 (2011). https://doi.org/10.1063/1.3521268
85. E.E. Fileti, Hd.A. Chagas, G. Colherinhas, T. Malaspina, Quantum molecular dynamics approach to understanding interactions in betaine chloride and amino acid natural deep eutectic solvents. ACS Phys. Chem. Au **5**(1), 72–79 (2024). https://doi.org/10.1021/acsphyschemau.4c00072
86. S. Paul, S. Paul, The influence of trehalose on hydrophobic interactions of small nonpolar solute: a molecular dynamics simulation study. J. Chem. Phys. **139**(4), 044508 (2013). https://doi.org/10.1063/1.4816521
87. P.T. Sodré, A.M. Aguilar, W.A. Alves, M.D. Coutinho-Neto, Intrinsic and environmental modulation of stereoselective aldol organocatalyzed reactions by proline-containing lipopeptides. RSC Adv. **14**(29), 21035–21046 (2024). https://doi.org/10.1039/d4ra03222e
88. B. Bhaskararao, R.B. Sunoj, Two chiral catalysts in action: insights into cooperativity and stereoselectivity in proline and *Cinchona*-thiourea dual organocatalysis. Chem. Sci. **9**(46), 8738–8747 (2018). https://doi.org/10.1039/c8sc03078b
89. H. Yang, M.W. Wong, (S)-proline-catalyzed nitro-Michael reactions: towards a better understanding of the catalytic mechanism and enantioselectivity. Org. Biomol. Chem. **10**(16), 3229–3235 (2012). https://doi.org/10.1039/c2ob06993h
90. S. Zárate-Roldán, M.J. Trujillo-Rodríguez, M.C. Gimeno, R.P. Herrera, L-proline-based deep eutectic solvents as green and enantioselective organocatalyst/media for aldol reaction. J. Mol. Liq. **396**, 123971 (2024). https://doi.org/10.1016/j.molliq.2024.123971

Publisher's Note Springer Nature remains neutral with regard to jurisdictional claims in published maps and institutional affiliations.